Editors' Suggestion

Fluid dynamics of a liquid mirror space telescope

Israel Gabay,[1] Omer Luria,[1] Edward Balaban,[2] Amir D. Gat,[1,*] and Moran Bercovici[1,†]
[1]*Faculty of Mechanical Engineering, Technion – Israel Institute of Technology, Haifa, Israel*
[2]*NASA Ames Research Center, Moffett Blvd., Moffett Field, California, USA*

(Received 8 July 2025; accepted 30 March 2026; published 16 June 2026)

Large aperture telescopes are pivotal for exploring the universe, yet even with state-of-the-art manufacturing and launch technology, their size is limited to several meters. As we aim to build larger telescopes—extending tens of meters—designs in which the main mirror is based on liquid deployment in space are emerging as promising candidates. However, alongside their enormous potential advantages, liquid-based surfaces present new challenges in material science, mechanics, and fluid dynamics. One of the fundamental questions is whether it is possible for such surfaces to maintain their precise optical shape over long durations, and in particular under the forces induced by the telescope's accelerations. In this paper, we present a model and a closed-form analytical solution for the non-self-adjoint problem of the dynamics of a thin liquid film pinned within a finite circular domain. We use the 50-m Fluidic Telescope concept as the case study and examine the liquid dynamics of the telescope under both slewing actuation and relaxation regimes, elucidating the role of geometrical parameters and liquid properties. The solutions reveal a maneuvering "budget" wherein the degradation of the mirror surface is directly linked to the choice of maneuvers and their sequence. By simulating 10 years of typical operation, we show that, while the maximal deformation might reach several microns, the spatial distribution and propagation rate of the deformation allow the telescope to maintain its optical functionality for years, with at least a substantial portion of the aperture remaining suitable for astronomical observations. The model provides valuable insights and guidelines into the performance of liquid-film space telescopes, marking a crucial step toward realizing the potential of this innovative concept.

DOI: 10.1103/dpk3-4256

I. INTRODUCTION

Are we alone in the universe? This question captivates astrophysicists and space researchers worldwide [1,2]. Space telescopes with apertures of tens of meters in diameter (and thus capable of sufficiently detailed observations of extrasolar planets) could be a key tool in solving this mystery [3–5]. However, despite significant advances in space telescope technologies, constructing such large apertures remains extremely challenging [6,7].

The largest operational space telescope, the James Webb Space Telescope (JWST), launched in 2021, has a primary mirror of 6.5 m in diameter and yields an order of magnitude improvement in light collection compared to the previous flagship telescope, the Hubble Space Telescope [8,9]. JWST is one of the most expensive single-piece engineering projects in the world. For this mission, NASA used a launch vehicle with one of the largest payload bays available (Ariane 5) [10,11],

*Contact author: amirgat@technion.ac.il
†Contact author: mberco@technion.ac.il

in combination with the segmented main mirror, which was launched folded and then deployed in space. However, the segmentation approach cannot be realistically scaled to tens of meters [6,12].

In recent years, there has been growing interest in liquid-based optical components [13–15] for both ground and space telescopes, due to the nature of liquid interfaces which provides smooth and continuous surfaces. The concept of liquid-based ground telescope dates back to Newton [16,17] who suggested that a rotating liquid metal tank with a base perpendicular to the gravitational field would shape the liquid interface into a paraboloid surface [18,19]. Technological challenges prevented Newton from implementing such a telescope, and it became a reality only in the late 19th century [17,20]. Although the optical quality of such telescopes can be good, they suffer from several major limitations. First and foremost, such a telescope can point only in the zenith direction (normal to the surface of the Earth) and cannot be slewed without losing its parabolic shape and thus its optical functionality. A second limitation is on size, as accurately controlling the rotation of larger mirrors becomes a significant technological challenge. While operation by rotation requires gravity and thus is more suitable for ground telescopes (either on Earth or, e.g., on the Moon), implement a rotating space telescope where the role of gravity is achieved by acceleration along the rotation axis.

The Zenith project [13,21,22], led by the Defense Advanced Research Projects Agency, aims to create slewable Earth-based liquid mirror telescopes. The general approach taken by all the participating teams so far is control of the mirror surface through electromagnetic fields. Recently Rowlands *et al.* [22] presented their steady-state model for the topography of a liquid telescope under magnetic actuation which induces normal stresses at the liquid-fluid interface. By assuming that the liquid film reaches a static hydromagnetic state they solve for the liquid topography under the influence of gravity, surface tension, and the Maxwell stress resulting from the magnetic fields.

The Fluidic Telescope (FLUTE) project [23–25], which the authors of this paper are associated with, takes a different approach to creating a liquid-mirror telescope. The project—a joint effort between NASA and Technion—has a goal of creating space telescopes with mirrors measuring in tens of meters in diameter. In the FLUTE approach, the reflecting surface is created with a thin liquid film which, in microgravity, will naturally acquire a spherical shape corresponding to its minimum energy state. Frumkin *et al.* [26] and Elgarisi *et al.* [27] have provided analytical solutions for the steady-state shape of such a film, as a function of its liquid volume and boundary conditions. Based on this theoretical framework, one can consider surface corrections for the minimum energy surface through active liquid actuation. However, even in the absence of such actuation, the FLUTE approach must account for liquid dynamics as the telescope slews to different astronomical targets and performs orbit maintenance maneuvers, thus subjecting the liquid to perturbations.

Regardless of the specific approach, from a fluid mechanics perspective, the problem of a liquid-based space telescope can be considered as a finite volume of liquid maintained within a circular domain. While steady-state computations are an important first step in understanding the potential of such systems, film dynamics cannot be neglected when considering the actual operation of actuation devices. We provide, for the first time, a theoretical model and an analytical solution for film dynamics in a finite circular domain. We use the FLUTE approach as the case study of space-based liquid mirror dynamics and study the telescope's response to one of the most significant sources of perturbations for a space telescope—its own slewing maneuvers required for changing its line of sight in space. Moreover, the same finite-domain thin-film framework is also relevant for terrestrial liquid-based adaptive optics, where a confined and pinned liquid interface is actively shaped to correct wavefront errors in imaging systems, including optofluidic adaptive optics and microscope implementations [28–30].

In this work, we use the model to gain insight into the liquid dynamics resulting from slewing maneuvers and offer simplified expressions to predict film deformations based on geometrical parameters, liquid properties, and maneuver characteristics, using a nondimensional analysis of the actuation and relaxation stages. Furthermore, we simulate 10 years of operation of such a hypothetical telescope and show that, while the maximum deformation can reach thousands of nanometers (for a telescope 50 m in diameter with a 1-mm film thickness), the rate of propagation

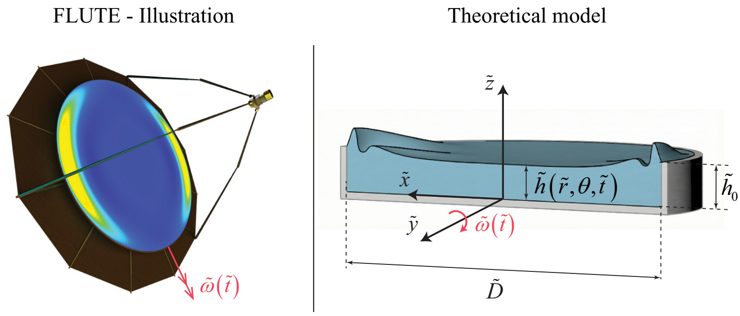

FIG. 1. Schematic representation of the FLUTE concept and the theoretical model. Left: Artistic impression of the FLUTE telescope in space during a slewing maneuver. The primary mirror, composed of a thin liquid film, undergoes deformation as a result of the angular velocity. Right: Illustration of the theoretical framework: a thin liquid film of thickness $\tilde{h}(\tilde{r},\theta,\tilde{t})$ is pinned within a flat circular frame of diameter $\tilde{D}$ and initial thickness $\tilde{h}_0$. The film is subjected to an angular velocity $\tilde{\omega}(\tilde{t})$ around the $\tilde{y}$ axis, simulating the slewing maneuver. The coordinate system is centered at the base of the chamber. Note that the film thickness and subsequent deformations are not drawn to scale. In practice, the film thickness is four orders of magnitude smaller than the chamber diameter, and deformations are four to six orders of magnitude smaller than the film thickness.

of these disturbances toward the center of the telescope remains slow enough to allow for years of operation with a substantial portion of its aperture remaining suitable for high-quality astronomical observations.

II. THE FLUIDIC TELESCOPE MODEL

Figure 1 illustrates the FLUTE concept and the theoretical model used in this work. The primary mirror is made of a thin liquid film confined within a circular frame. In the actual telescope design the film would be supported on a spherical substrate with aperture diameter $\tilde{D}$ and radius of curvature $\tilde{R}_c$. Howell [31] introduced a dimensionless parameter that quantifies the surface slope, $\epsilon = \tilde{D}/(2\tilde{R}_c)$ and explored the thin film equation under different limits of this parameter. For $\epsilon \ll 1$, the leading-order dynamics reduce to the planar lubrication model used here, where appears. Consequently, we model the telescope as a flat circular chamber of diameter $\tilde{D}$ and height $\tilde{h}_0$, filled with a liquid of mass density $\tilde{\rho}$, dynamic viscosity $\tilde{\mu}$, and surface tension $\tilde{\sigma}$, as shown in the right panel of Fig. 1. The coordinate origin is at the center of the chamber floor, with $\tilde{z}$ normal to the floor and $(\tilde{x}, \tilde{y})$ spanning the chamber plane. We consider slewing maneuvers in which the chamber rotates with angular velocity $\tilde{\omega}$ about an in plane axis passing through the chamber center. Under the shallow geometry assumption, $\tilde{h}_0 \ll \tilde{D}$, and negligible inertia, $\mathrm{Re}_r \ll 1$, the momentum equations reduce to the lubrication equations [32],

$$\tilde{\boldsymbol{\nabla}}_s \tilde{p} = \tilde{\mu} \frac{\partial^2 \tilde{\mathbf{u}}_s}{\partial \tilde{z}^2} - \tilde{\rho} \tilde{\mathbf{a}}_s, \tag{1a}$$

$$\frac{\partial \tilde{p}}{\partial \tilde{z}} = -\tilde{\rho}(\tilde{g} + \tilde{a}_z), \tag{1b}$$

while the continuity equation (mass conservation) can be written as

$$\tilde{\boldsymbol{\nabla}}_s \cdot \tilde{\mathbf{u}}_s + \frac{\partial \tilde{u}_z}{\partial \tilde{z}} = 0. \tag{2}$$

Here the subscripts s and z denote components parallel and normal to the chamber floor, respectively, and $\tilde{\mathbf{a}}$ is the acceleration of the noninertial reference frame. Within the scope of this work, we limit the acceleration, $\tilde{\mathbf{a}}$, to include only body forces due to the slewing maneuver itself. The term g in the z equation can be used to further account for the Earth's gravity in simulations of terrestrial liquid dynamics but is otherwise set to zero in all space applications. Finally, for simplicity and without loss of generality, we consider rotation about the $\tilde{y}$ axis, $\tilde{\boldsymbol{\omega}} = \tilde{\omega}(\tilde{t})\hat{\mathbf{y}}$, as shown in Fig. 1. The system acceleration is then

$$\tilde{\mathbf{a}} = \tilde{g}\hat{\mathbf{z}} - 2\tilde{\omega}\tilde{u}\hat{\mathbf{z}} + 2\tilde{\omega}\tilde{w}\hat{\mathbf{x}} - \tilde{\omega}^2\tilde{x}\hat{\mathbf{x}} - \tilde{\omega}^2\tilde{z}\hat{\mathbf{z}} - \dot{\tilde{\omega}}\tilde{x}\hat{\mathbf{z}} + \dot{\tilde{\omega}}\tilde{z}\hat{\mathbf{x}}. \tag{3}$$

Substituting the system acceleration into the momentum equations yields

$$\tilde{\boldsymbol{\nabla}}_s\tilde{p} = \tilde{\mu}\frac{\partial^2\tilde{\mathbf{u}}_s}{\partial\tilde{z}^2} + \tilde{\rho}(-2\tilde{\omega}\tilde{w} - \dot{\tilde{\omega}}\tilde{z} + \tilde{\omega}^2\tilde{x})\hat{\mathbf{x}}, \tag{4a}$$

$$\frac{\partial\tilde{p}}{\partial\tilde{z}} = \tilde{\rho}(\tilde{\omega}^2\tilde{z} + 2\tilde{\omega}\tilde{u} + \dot{\tilde{\omega}}\tilde{x} - \tilde{g}). \tag{4b}$$

The negligible inertia limit requires $\tilde{\omega}_0 \ll \tilde{\nu}/\tilde{h}_0^2$. This bound also implies that the Coriolis terms are negligible, as can be seen by comparing their magnitude to that of the centrifugal term in Eq. (4a). Similarly, requiring $\dot{\tilde{\omega}} \ll \tilde{\omega}_0^2/\varepsilon$ ensures that the Euler terms are negligible. A full nondimensionalization and evaluation of these bounds using the FLUTE parameters is given in Appendix A. With these bounds, the momentum equations simplify to

$$\tilde{\boldsymbol{\nabla}}_s\tilde{p} = \tilde{\mu}\frac{\partial^2\tilde{\mathbf{u}}_s}{\partial\tilde{z}^2} + \tilde{\rho}\tilde{\omega}^2\tilde{x}\hat{\mathbf{x}}, \tag{5a}$$

$$\frac{\partial\tilde{p}}{\partial\tilde{z}} = -\tilde{\rho}\tilde{g}. \tag{5b}$$

To derive the evolution equation representing the film height dynamics, we integrate the in plane momentum equation [Eq. (5a)] with respect to $\tilde{z}$ twice and apply the no slip and no tangential stress boundary conditions at the lower and upper interfaces, respectively,

$$\tilde{\mathbf{u}}_s = \frac{1}{2\tilde{\mu}}(\tilde{\boldsymbol{\nabla}}_s\tilde{p} - \tilde{\rho}\tilde{\omega}^2\tilde{x}\hat{\mathbf{x}})(\tilde{z}^2 - 2\tilde{z}\tilde{h}). \tag{6}$$

Solving the perpendicular momentum equation [Eq. (5b)] and using the normal stress balance at the free surface, we obtain the pressure distribution in the liquid film,

$$\tilde{p} - \tilde{p}_0 = -\tilde{\sigma}\tilde{\nabla}^2\tilde{h} + \tilde{\rho}\tilde{g}\tilde{h} - \tilde{\rho}\tilde{g}\tilde{z}, \tag{7}$$

where $\tilde{p}$ and $\tilde{p}_0$ are the pressure of the liquid and the environment, respectively. Using the kinematic condition, $\tilde{h}_{\tilde{t}} + \tilde{\boldsymbol{\nabla}}_s \cdot \int_0^{\tilde{h}} \tilde{\mathbf{u}}_s d\tilde{z} = 0$, and substituting the velocity profile and liquid pressure we obtain the well-known thin-film evolution equation [33,34],

$$\tilde{h}_{\tilde{t}} = \frac{1}{3\tilde{\mu}}\tilde{\boldsymbol{\nabla}}_s \cdot [\tilde{h}^3(\tilde{\boldsymbol{\nabla}}_s(-\tilde{\sigma}\tilde{\nabla}^2\tilde{h} + \tilde{\rho}\tilde{g}\tilde{h}) - \tilde{\rho}\tilde{\omega}^2\tilde{x}\hat{\mathbf{x}})]. \tag{8}$$

By further assuming small deformations (compared to the liquid mirror thickness), $\tilde{d} \ll \tilde{h}_0$, and defining the following nondimensional variables, $\tilde{t} = \tilde{\tau}t$, $\tilde{r} = r\tilde{D}/2$, $\tilde{d} = d\tilde{h}_0$, we obtain the linearized deformation equation,

$$d_t + \nabla_s^4 d - \mathrm{Bo}\nabla_s^2 d = -A\omega^2(t), \tag{9}$$

where we define $\tilde{\tau} = \frac{3\tilde{\mu}\tilde{D}^4}{16\tilde{h}_0^3\tilde{\sigma}}$, $\mathrm{Bo} = \frac{\tilde{\rho}\tilde{g}\tilde{D}^2}{4\tilde{\sigma}}$, and $A = \frac{\tilde{\rho}\tilde{\omega}_0^2\tilde{D}^4}{16\tilde{\sigma}\tilde{h}_0}$. The second term of the left-hand side of the nondimensional evolution equation (the capillary forces term) is negligible compared to the source term, yet we must account for it, as it is the highest-order term, and thus is needed to satisfy the boundary conditions. Consequently, near the edges, there is a narrow boundary-layer region in which the capillary forces are important.

As shown in Fig. 1, we examine a closed chamber with rigid walls at its boundaries. Due to the chamber geometry, the film must be pinned at the edges, meaning $\tilde{h} = \tilde{h}_0$ at the boundary. Additionally, due to the rigid walls at the chamber perimeter, the in-plane velocity, $\tilde{\mathbf{u}}_s = 0$, must vanish at the boundary. Thus, integrating the velocity profile, Eq. (6), with respect to $\tilde{z}$, evaluating the expression at the boundary, and taking only the radial component gives:

$$\tilde{p}_{\tilde{r}} = \tilde{\rho}\tilde{\omega}^2\tilde{r}^2\cos^2\theta. \tag{10}$$

Substituting this pressure condition into Eq. (7), the liquid's pressure, yields the no penetration boundary condition in terms of the film height, and thus the system boundary conditions, at $\tilde{r} = \tilde{D}/2, \theta,$ and $\tilde{t} \geqslant 0$ are as follows:

$$\begin{aligned} &\tilde{h} = \tilde{h}_0, \\ &\tilde{h}_{\tilde{r}\tilde{r}\tilde{r}} - \frac{1}{\tilde{r}^2}\tilde{h}_{\tilde{r}} + \frac{1}{\tilde{r}}\tilde{h}_{\tilde{r}\tilde{r}} - \frac{2}{\tilde{r}^3}\tilde{h}_{\theta\theta} + \frac{1}{\tilde{r}^2}\tilde{h}_{\tilde{r}\theta\theta} + \tilde{\rho}\tilde{g}\tilde{h}_r = -\frac{\tilde{\rho}\tilde{\omega}_0^2\tilde{r}}{\tilde{\sigma}}\omega^2(\tilde{t})\cos^2\theta, \end{aligned} \tag{11}$$

which in terms of the surface deformation for nondimensional variables form the boundary conditions,

$$\begin{aligned} &d = 0, \\ &d_{rrr} + (\mathrm{Bo} - 1)d_r + d_{rr} - 2d_{\theta\theta} + d_{r\theta\theta} = -A(\omega(t)\cos\theta)^2 \end{aligned} \tag{12}$$

at $r = 1, \theta,$ and $t \geqslant 0$.

A. Analytical solution

The evolution of the film deformation is governed by a linear fourth-order partial differential equation [Eq. (9)] and is subject to boundary conditions imposed at the chamber edge, (12), and an arbitrary initial deformation profile. Gabay *et al.* showed that a one-dimensional (1D) pinned thin film problem in a closed chamber forms a non-self-adjoint problem [35]. The 2D case we study here has similar mathematical characteristics. This adds complexity to the solution procedure, particularly in constructing a complete basis for projection of arbitrary inputs. To address this, we employ a generalized separation of variables method adapted for non-self-adjoint systems [36].

The first step is to homogenize the boundary conditions. The centrifugal forcing that appears in the no penetration condition at the chamber, (12), introduces an azimuthal dependence, which precludes direct application of the separation of variables method. To overcome this, we define a new variable, $\delta(r, \theta, t)$, such that

$$d(r, \theta, t) = \delta(r, \theta, t) + f(r, \theta)g(t), \tag{13}$$

where $d(r, \theta, t)$ is the film deformation,

$$f(r, \theta) = \sum_{n=0}^{N} C_n r^n A \frac{\cos(2\theta) + 1}{2}, \tag{14}$$

is the spatial auxiliary function, and $g(t) = \omega^2(t)$ is the time-dependent part. These functions are chosen such that the boundary conditions for δ are homogeneous and such that substituting this variable into the governing equation yields a right-hand side that is free of singularities in both the radial and azimuthal directions. The set of coefficients used to enforce these requirements are (a full derivation is provided in Appendix B),

$$
\begin{aligned}
&C_0 = 0, \quad C_1 = 0, \quad C_2 = -\frac{339+\mathrm{Bo}}{22(192+\mathrm{Bo})}, \quad C_3 = 0,\\
&C_4 = \frac{21(287+\mathrm{Bo})}{44(192+\mathrm{Bo})}, \quad C_5 = 0, \quad C_6 = -\frac{35(243+\mathrm{Bo})}{11(192+\mathrm{Bo})},\\
&C_7 = \frac{63(224+\mathrm{Bo})}{11(192+\mathrm{Bo})}, \quad C_8 = -\frac{175(207+\mathrm{Bo})}{44(192+\mathrm{Bo})}, \quad C_9 = 1.
\end{aligned}
\tag{15}
$$

Substituting this decomposition into the PDE system, Eqs. (9) and (12), transforms the system into a homogeneous PDE for $\delta(r, \theta, t)$,

$$
\delta_t + \nabla_s^4\delta - \mathrm{Bo}\nabla_s^2\delta = -g_t f(r,\theta) - g\big(A + \nabla_s^4 f - \mathrm{Bo}\nabla_s^2 f\big),
\tag{16}
$$

with boundary conditions for $t \geqslant 0$ at $r = 1, \theta$,

$$
\begin{aligned}
&\delta = 0,\\
&\delta_{rrr} + (\mathrm{Bo}-1)\delta_r + \delta_{rr} - 2\delta_{\theta\theta} + \delta_{r\theta\theta} = 0
\end{aligned}
\tag{17}
$$

and an initial condition

$$
\delta(r,\theta,0) = d(r,\theta,0) - f(r,\theta)g(0).
\tag{18}
$$

We then assume a separable solution of the form $\delta(r,\theta,t) = R(r)\Theta(\theta)T(t)$. We guess the azimuthal component solution for a periodic domain, with eigenfunctions $\Theta_n = a_n\cos(n\theta) + b_n\sin(n\theta)$. These form a complete orthogonal basis in the azimuthal direction. Substituting these into the linear PDE and dividing by δ yields two ordinary differential equations, one in r and one in t, each equated to a constant separation parameter,

$$
\begin{aligned}
-\frac{T'}{T} = \lambda^4 = {}& \frac{r^4R^{(4)} + 2r^3R^{(3)} - r^2R'' + rR'}{Rr^4} + \frac{-n^2(4R - 2rR' + r^2R'' - \mathrm{Bo}r^2R)}{Rr^4}\\
&+ \frac{-\mathrm{Bo}(r^4R'' + r^3R') + n^4R}{Rr^4}.
\end{aligned}
\tag{19}
$$

The radial component results in a fourth-order differential equation with coefficients that depend on r, involving combinations of Bessel and modified Bessel operators and can be presented in a more compact form:

$$
L_2[L_1[R]] = 0,
\tag{20}
$$

where $L_1 = \partial_{rr} + \frac{\partial_r}{r} - (\frac{n^2}{r^2} + \lambda^2)$ and $L_2 = \partial_{rr} + \frac{\partial_r}{r} - (\mathrm{Bo} + \frac{n^2}{r^2} - \lambda^2)$. The eigenfunctions R satisfy boundary conditions corresponding to zero deformation and zero net flow at the domain edge, along with regularity at the center,

$$
R(1) = 0,
\tag{21a}
$$

$$
R^{(3)}(1) + R''(1) - (1 + \mathrm{Bo} + n^2)R'(1) = 0,
\tag{21b}
$$

$$
|R(0)| < \infty.
\tag{21c}
$$

Solving Eq. (19) and applying these conditions yields the transcendental equation for the radial eigenvalues,

$$
\alpha\beta^2 J_{n-1}(\alpha) = [\alpha^2 + \beta^2]n + \beta\alpha^2\frac{I_{n-1}(\beta)}{I_n(\beta)}J_n(\alpha),
\tag{22}
$$

and the eigenfunctions of the system,

$$R_{nm}(r) = \begin{cases} J_n(\alpha_{nm} r) - \frac{J_n(\alpha_{nm})}{I_n(\beta_{nm})} I_n(\beta_{nm} r) & n \geqslant 0, m > 0 \\ 0 & n > 0, m = 0 \\ \frac{I_0(\sqrt{\mathrm{Bo}} r)}{1 - I_0(\sqrt{\mathrm{Bo}})} & n = 0, m = 0, \end{cases} \tag{23}$$

where $\alpha_{nm} = \sqrt{-\mathrm{Bo} + \sqrt{\mathrm{Bo}^2 + 4\lambda_{nm}^4}}$ and $\beta_{nm} = \sqrt{\mathrm{Bo} + \sqrt{\mathrm{Bo}^2 + 4\lambda_{nm}^4}}$.

Among the radial eigenfunctions, the eigenfunction of $n = m = 0$ corresponds to the steady-state solution. In the limit of zero Bond number (i.e., in the absence of gravity), the $n = m = 0$ eigenfunction is no longer valid and the actual steady-state solution takes the form of a parabolic profile. This is consistent with the spherical shape expected for a free interface in microgravity and follows naturally from the linearization procedure used to derive the governing equation.

To project arbitrary initial conditions or source terms onto the system eigenfunction in the case of a non-self-adjoint problem, we must construct the adjoint problem. While the azimuthal operator and boundary conditions (periodicity) are self-adjoint and the azimuthal eigenfunctions form an orthogonal set, the full system is not. In particular, the radial eigenfunctions are not orthogonal under the standard inner product of a cylindrical coordinate system, $\langle U, V\rangle_r = \int_0^1 UV r dr$, where U and V are two distinct radial eigenfunctions.

Thus, following the procedure presented in Ref. [35], we should define the complementary boundary conditions, which are the boundary conditions of the adjoint problem. To do so, we use the biorthogonality relation [36], $\langle L[R], Y\rangle_r = \langle R, L^*[Y]\rangle_r$, where Y is an adjoint eigenfunction, and L^* is the adjoint operator, which in this case is the same as the original operator as Bessel and modified Bessel operators are self-adjoint. Now, by integrating the biorthogonality relation by parts over the domain, we find the boundary conditions of the adjoint system:

$$Y'(1) = 0, \tag{24a}$$

$$Y'''(1) - n^2 Y'(1) = 0, \tag{24b}$$

$$|Y(0)| < \infty, \tag{24c}$$

which the first two resulted from the biorthogonality relation and the third is the regularity condition at the chamber's center. Solving the same differential operator [Eq. (19)] but with the adjoint boundary conditions yields the adjoint eigenfunctions

$$Y_{nm} = \begin{cases} 0 & n > 0, m = 0 \\ J_n(\alpha_{nm}) + \Pi(n, m) I_n(\beta_{nm}) & n \geqslant 0, m > 0, \\ \mathrm{const} & n = 0, m = 0 \end{cases} \tag{25}$$

where $\Pi(n, m) = \frac{\alpha_{nm}}{\beta_{nm}} \frac{J_{n-1}(\alpha_{nm}) - J_{n+1}(\alpha_{nm})}{I_{n-1}(\beta_{nm}) + I_{n+1}(\beta_{nm})}$.

To construct the film deformation solution, we substitute the separation of variables expression,

$$\delta(r, \theta, t) = \sum_{n=0}^{\infty} \sum_{m=0}^{\infty} R_{nm}(r)\Theta_n(\theta) T_{nm}(t), \tag{26}$$

into Eq. (16) and obtain the first-order differential equation for the temporal eigenfunctions,

$$\begin{aligned} &\sum_{n=0}^{\infty} \sum_{m=0}^{\infty} R_{nm}\Theta_n T'_{nm} + \sum_{n=0}^{\infty} \sum_{m=0}^{\infty} \nabla_z^4 (R_{nm}\Theta_n) T_{nm} - \mathrm{Bo} \sum_{n=0}^{\infty} \sum_{m=0}^{\infty} \nabla_z^2 (R_{nm}\Theta_n) T_{nm} \\ &\quad = \sum_{n=0}^{\infty} \sum_{m=0}^{\infty} R_{nm}\Theta_n a_{nm}(t) + \sum_{n=0}^{\infty} \sum_{m=0}^{\infty} R_{nm}\Theta_n b'_{nm}(t), \end{aligned} \tag{27}$$

where the right-hand side of Eq. (16) and its initial condition are expressed in terms of a double series of the system eigenfunctions:

$$\begin{aligned}\sum_{n=0}^{\infty}\sum_{m=0}^{\infty} R_{nm}\Theta_n a_{nm} &= -g\big(A+\nabla_s^4 f-\mathrm{Bo}\nabla_s^2 f\big),\\ \sum_{n=0}^{\infty}\sum_{m=0}^{\infty} R_{nm}\Theta_n b_{nm} &= -g_t f(r,\theta),\\ \sum_{n=0}^{\infty}\sum_{m=0}^{\infty} R_{nm}\Theta_n I_{nm} &= \delta(r,\theta,0).\end{aligned} \tag{28}$$

The main issue one should be aware of while solving a non-self-adjoint problem using this method, is expressing each one of the terms in (27) as a series of the system eigenfunctions. In contrast to the self-adjoint case, to express an arbitrary function, $\phi(r,\theta)$, in terms of the system spatial eigenfunctions, here we use the adjoint eigenfunctions:

$$\phi(r,\theta)=\sum_{n=0}^{\infty}\sum_{m=0}^{\infty} c_{nm}R_{nm}(r)\Theta_n(\theta),\ c_{nm}=\frac{\int_0^{2\pi}\int_0^1 Y_{nm}\Theta_n\phi(r,\theta)rdrd\theta}{\int_0^{2\pi}\int_0^1 Y_{nm}R_{nm}(r)\Theta_n^2(\theta)rdrd\theta}. \tag{29}$$

Thus, the solution for each time-dependent function is obtained in the same manner,

$$T_{nm}=\int_{s=0}^{t} e^{\lambda_{nm}^4(s-t)}(a_{nm}(s)-b_{nm}(s))ds+I_{nm}e^{-\lambda_{nm}^4 t}, \tag{30}$$

where

$$\begin{aligned} a_{nm}(t) &= -\frac{\int_0^{2\pi}\int_0^1 Y_{nm}\Theta_n g(t)(A+\nabla_z^4 f-\mathrm{Bo}\nabla_z^2 f)rdrd\theta}{\int_0^{2\pi}\int_0^1 Y_{nm}R_{nm}(r)\Theta_n^2(\theta)rdrd\theta},\\ b_{nm}(t) &= -\frac{\int_0^{2\pi}\int_0^1 Y_{nm}\Theta_n g_t(t)f(r,\theta)rdrd\theta}{\int_0^{2\pi}\int_0^1 Y_{nm}R_{nm}(r)\Theta_n^2(\theta)rdrd\theta},\\ I_{nm} &= -\frac{\int_0^{2\pi}\int_0^1 Y_{nm}\Theta_n\delta(r,\theta,0)rdrd\theta}{\int_0^{2\pi}\int_0^1 Y_{nm}R_{nm}(r)\Theta_n^2(\theta)rdrd\theta}.\end{aligned} \tag{31}$$

III. EXPERIMENTAL VALIDATION

Validating the mathematical model with a demonstration of a slewing telescope in conditions of microgravity was not practical. Therefore, we performed an alternative experiment under normal laboratory conditions (i.e., in the presence of gravity), taking advantage of the fact that the mathematical model accounts for gravitational acceleration as a parameter. This allows direct comparison between the experimental results and theoretical predictions at the relaxation regime, even though the manuscript focuses on a space telescope intended for microgravity environments.

To validate the model in the laboratory setting, we sought a contact-free approach to impose an arbitrary initial deformation on the surface (one which is complex, and thus accounts for multiple modes) and observe its relaxation dynamics over time. To achieve this, we selected dielectrophoresis (DEP), which can induce a contactless force via electrodes located at the bottom of the film. The experimental setup consisted of a microfabricated circular chamber, with a diameter of 3.8 mm and a height of 50 µm, which was filled with 0.57 µl silicone oil with a density of 970 kg/ m^3 and a surface tension of 20 mN m^{-1}. DEP forces were applied through surface electrodes prepatterned at the base of the chamber [37].

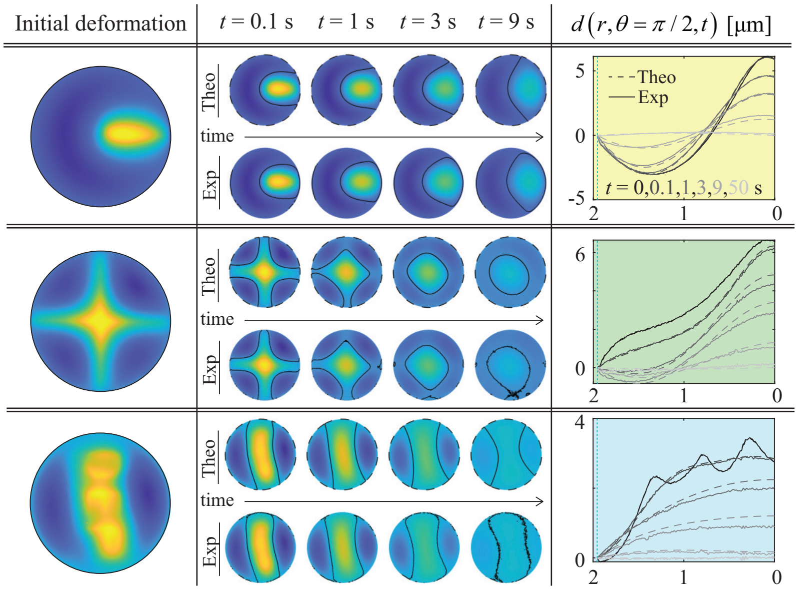

FIG. 2. Experimental validation of the theoretical model for three different initial conditions. We deform the surface using DEP forces and use the resulting deformation as an initial condition to our model, which predicts the relaxation dynamics of the liquid-air interface. We compare the predictions to those measured in the experiment after the DEP forcing is released. The left column shows the initial deformation of each case. In the middle column, theoretical solution (upper row) and experimental measurements (lower row) are depicted for $t = 0.1$, 1, 3, and 9 s. The black contour in each map indicates the zero-deformation contour line. The right column presents a two-dimensional cross-section view along the radial direction at $\theta = \pi/2$, showing good agreement between the theoretical (dashed lines) and experimental (solid lines) deformation profiles at multiple times ($t = 0$, 0.1, 1, 3, 9, 50 s). Grayscale color coding differentiates the timing of measurements, with the initial deformation depicted in black and later measurements in progressively lighter shades.

Each experiment began by applying an electric field, allowing the liquid to stabilize in its new electrohydrostatic state. When the voltage is turned off, the liquid undergoes relaxation, and we record the spatial deformation as a function of time using a digital holographic microscope (DHM Lyncee Tec R1000, 1.25× microscope objective).

Figure 2 illustrates the surface deformation from three distinct experiments, depicting three different initial shapes in the left column. In all cases, we allow the interface to reach a steady state, and all deformation data presented here is obtained by subtracting the steady-state topography from the topography data of any other time point. In the middle column, interfacial deformation is plotted at four time points for each case, for both the experiments and the theoretical predictions. A contour line at $d = 0$ is marked to guide the eye in comparison of the results. The right column offers quantitative comparisons by displaying cross sections of the deformation maps at $\theta = \pi/2$, for both the theoretical (dashed line) and experimental (solid line) results. Throughout, the theoretical model shows good agreement with the experimental results.

IV. LIQUID MIRROR DEFORMATION

In the analytical model section, we provided a nondimensional analytical solution of the film deformation. The nondimensional representation is the most generic one, as it allows us to obtain insights onto the various timescales of the observed phenomenon, and its parametric representation allows computation for any desired configuration. However, it is also instructive to consider several

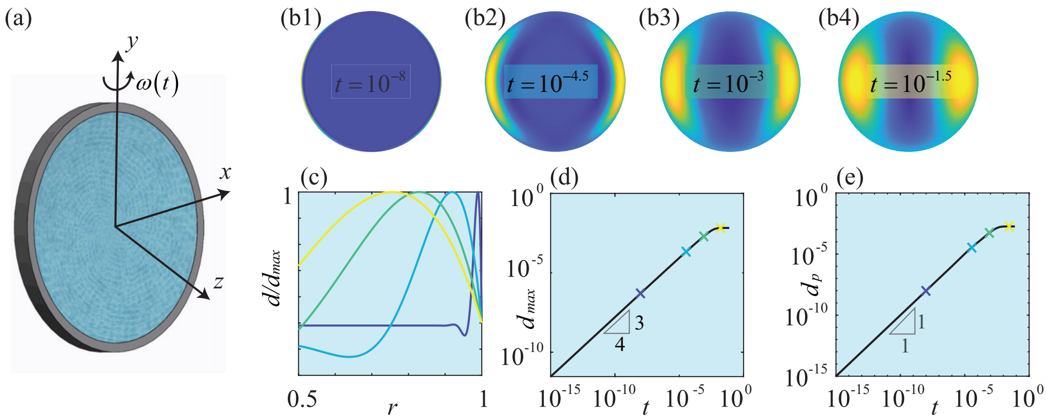

FIG. 3. Nondimensional analysis of the liquid film's deformation dynamics due to a continuous slewing maneuver. (a) Illustration of the telescope setup undergoing rotation around the y axis. [(b1)–(b4)] The deformation map at four different times, which span 6.5 orders of magnitude, showing the progression of the deformation from the telescope edges [barely visible in (b1)] toward its center. (c) The deformation along the radial direction coinciding with the x axis at the same time points depicted in (b). [(d) and (e)] Maximal and piston deformations as a function of time on a logarithmic scale, identifying a scaling relation for the early time dynamics of $d_{\max} \sim t^{3/4}$, and $d_p \sim t$ respectively. These relations hold for most of the actuation stage until late times. The "x" marks represent time steps corresponding to the plotted deformation maps in (b) and (c): $t = 10^{-8}$ dark blue, $t = 4.5 \times 10^{-4}$ light blue, $t = 10^{-3}$ green, and $t = 1.5 \times 10^{-1}$ yellow.

specific cases, to demonstrate how the model could be used to predict the behavior of a hypothetical liquid telescope undergoing multiple maneuvers during its operation. Thus, in this section we provide both the non-dimensional investigation and several dimensional case studies.

A. Nondimensional investigation

Figure 3 presents the deformation of the liquid mirror for the case of $A = 1$, resulting from a continuous slewing maneuver, $\vec{\omega}(t) = \omega_0\hat{y}$. As expected, the liquid is pushed towards the chamber edges along the x axis under this type of actuation. As shown in Figs. 3(b) and 3(c), at early times, the deformation builds up primarily within a narrow strip near the telescope's perimeter. The liquid is supplied from the center of the telescope, with the interface slowly receding while overall maintaining its spherical shape. We define this translation motion as "piston" (commonly used in optics to describe a uniform phase bias) deformation, $d_p = \frac{1}{\pi(0.8)^2}\int_0^{2\pi}\int_0^{0.8} d(r,\theta)\, r\, dr\, d\theta$. Although such a movement of the surface will introduce optical aberrations, those can usually be corrected by translating components along the optical axis. For this reason, surface piston is treated here as a deformation which does not restrict the telescope's performance. Figure 3(d) illustrates the maximum deformation as a function of time on a log-log scale, revealing a relation of $d_{\max} \sim t^{3/4}$ throughout most of the actuation period, until a steady-state deformation, illustrated in Fig. 3(b4), is achieved. Figure 3(e) shows the translation of the spherical surface maintained in an area within 80% of the total radius, i.e., the piston deformation.

Figure 4 shows the maximal deformation and the piston deformation, rescaled by $d_{\max}(t = 0.03)$ and $d_p(t = 0.03)$, respectively, as a function of time during the relaxation stage, following a slewing actuation with a duration of $t_a = 10^{-11}$ (blue line), $t_a = 10^{-9}$ (green line), and $t_a = 10^{-5}$ (yellow line). As illustrated in the figure, the relaxation stage of the liquid converges onto a single curve for both maximal and piston deformation, regardless of the duration of the actuation.

Figure 4(a) reveals three distinct regimes: immediately after the termination of the actuation, at very early times, we observe rapid decay corresponding to the highest wave numbers on the order

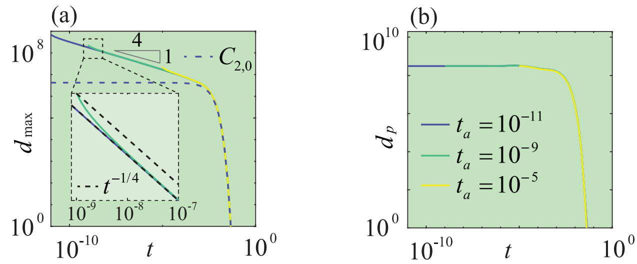

FIG. 4. The nondimensional maximal and piston deformations of the liquid mirror as a function of time after the telescope stops slewing, i.e., the relaxation stage. Panels (a) and (b) illustrate the maximal and piston deformations, respectively, as a function of time (normalized by the deformation at the last time point, $t = 0.03$) on a log-log scale. The different curves correspond to relaxations following actuations that began at $t = 0$ and ended at different times: $t_a = 10^{-11}$ (blue), $t_a = 10^{-9}$ (green), and $t_a = 10^{-5}$ (yellow). (a) At the earliest times (inset) we observe rapid decay corresponding to the dynamics of the fastest modes (shortest wavelengths). At intermediate times all curves coincide, and the decay follows a $t^{-1/4}$ dependence. At late times, the decay rate settles into that of the smallest wave number—the slowest mode ($n = 2, m = 0$). (b) The piston deformation is constant at both early and intermediate times and drops only when the higher modes decay and the shortest mode remains.

of 20% (as presented in the inset). At intermediate times (following the very early time and up to approximately 10^{-5}), the curves converge, and the decay of the maximum deformation follows a relation of $d_{\max} \sim t^{-1/4}$, in agreement with the dynamics previously suggested by Zhang *et al.* [38] for early-time behavior of healing capillary films. At later times, the decay of the maximum deformation corresponds to the dynamics of the longest wavelength (or the smallest eigenvalue) contributing to the deformation, which for the slewing maneuver type is the $\cos(2\theta)$ term that dominates the source term in Eq. (17). This mode is depicted as the dashed line in Fig. 4(a).

Under the FLUTE mission design concept, a telescope with a 50-m primary mirror and a liquid film of several millimeters in thickness, with a reference viscosity of 100 cSt and surface tension of 50 mN/m, has a characteristic system timescale on the order of 10^{14}. Thus, the entire operational timescale of a telescope, on the order of years, can be considered to be well within early- and intermediate-time regimes.

Using simulation results for both actuation and relaxation stages and the nondimensional system parameters, we can provide predictions for the maximal deformation and piston deformation as functions of the telescope's physical parameters. For the actuation regime, the maximal liquid deformation can be expressed as

$$\tilde{d}_{\max} = d_{\max}\tilde{h}_0 = AC_a t^{3/4}\tilde{h}_0, \tag{32}$$

where $C_a = 0.5192$ is a constant calculated from Fig. 4(d). By substituting the actuation time as a function of the angular velocity $\tilde{\omega}_0$, the requested slewing angle β, and the system timescale $\tilde{\tau}$, we obtain:

$$\tilde{d}_{\max,a} = \frac{C_a\tilde{\rho}\tilde{D}\tilde{\omega}_0^{5/4}\tilde{h}_0^{9/4}}{2\tilde{\sigma}^{1/4}}\left(\frac{\beta}{3\tilde{\mu}}\right)^{3/4}. \tag{33}$$

Similarly, the piston deformation can be expressed as $\tilde{d}_p = d_p\tilde{h}_0 = -At\tilde{h}_0$ and by substituting the actuation time as a function of $\tilde{\omega}_0$, β, and $\tilde{\tau}$, we obtain:

$$\tilde{d}_{p,a} = -\frac{\beta\tilde{h}_0^3\tilde{\rho}\tilde{\omega}_0}{3\tilde{\mu}}. \tag{34}$$

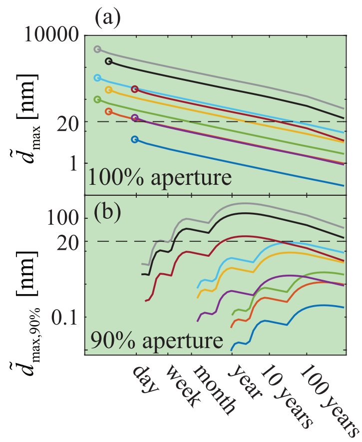

#N	$\tilde{h}_0$ [mm]	$\tilde{\omega}_0$ [μrad/s]	$\tilde{d}_{\max}$ [nm]
1	1	10	5.56
2	1	50	41.5
3	1	100	98.8
4	2	10	26.4
5	2	50	197
6	2	100	470
7	5	10	207
8	5	50	1553
9	5	100	3693

FIG. 5. Dimensional time-dependent deformation dynamics of a 50-m diameter liquid mirror during the relaxation phase, following a 45° slewing maneuver on a log-log scale. The table details the different experimental cases, specifying film thickness, angular velocity, and the resulting maximal deformation. Each row in the table corresponds to a curve in panels (a) and (b), with matching colors to facilitate easy comparison. (a) The maximal deformation over time for a full aperture. The circles correspond to deformations predicted by Eq. (33), aligning with the analytical solution. The horizontal dashed line at 20 nm serves as a reference, corresponding to $\tilde{\lambda}/20$ (where $\tilde{\lambda} = 400$ nm), an acceptable standard for high-quality space optics. The results show that regardless of the initial conditions, the deformation decays at the same rate at intermediate times. (b) The maximal deformation within a 90% aperture (i.e., the inner 45-m diameter aperture). While for the full aperture, the majority of cases exceed the 20-nm threshold, for the 90% aperture many cases remain below this mark for extended durations, since the deformations, while large, are confined to the outer regions of the telescope.

For the relaxation stage, neglecting the short decay at early times, the decay of the maximal deformation can be estimated using the relation $d_{\max} \sim t^{-1/4}$, i.e.,

$$\tilde{d}_{\max}(t) = \tilde{d}_{\max,a}\left(\frac{t_a}{t}\right)^{1/4}, \quad t \geqslant t_a, \tag{35}$$

where t_a is the slewing time and $\tilde{d}_{\max,a}$ is the maximal deformation obtained at the end of the actuation stage. The piston deformation remains constant at early and intermediate times. This is simply because, at these timescales, the deformation that began at the edges did not yet penetrate into the center of the telescope.

B. Dimensional investigation—Specific study cases

Here we present different case studies considering variation in film height, angular velocity, and maneuvering procedures, e.g., several maneuvers, different maneuvering angles, and variations in the axis of rotation. Yet, in all the cases considered here, we fix the properties of the liquid ($\tilde{\rho} = 1000$ kg/m^3, $\tilde{\nu} = 100$ cSt, $\tilde{\sigma} = 50$ mN/m) and the telescope diameter, $\tilde{D} = 50$ m.

Figure 5 presents the maximal deformation of the liquid mirror as a function of time after performing a 45° slewing maneuver. We investigate the influence of the film's thickness (ranging from 1 to 5 mm) and angular velocity (ranging from 10 to 100 μrad/s) on the deformation dynamics. Figure 5(a) shows the maximal deformation over the entire mirror, whereas Fig. 5(b) provides this value over the inner 90% of the telescope radius.

Since the slewing angle is identical across all configurations while the angular velocity varies, the actuation time differs between cases, causing the relaxation stage to begin at different times. The circles on each curve correspond to the deformation predicted by Eq. (33), which match well with the simulation results of the full analytical solution (30). The results also illustrate the $\tilde{\omega}_0^{5/4}$ and $\tilde{h}_0^{9/4}$ dependence of the maximal deformation predicted by Eq. (33). The horizontal dashed line represents a strict imperfection limit in astronomy at a value of 20 nm, corresponding to $\tilde{\lambda}/20$, where $\tilde{\lambda} = 400$ nm is the lower edge of the visible wavelength—a common figure for high-quality space optics. All curves decay at approximately the same rate, consistent with the observation in Fig. 4. In cases 7–9, where the film thickness is larger, the system's timescale is shorter ($\tilde{\tau} \approx 2 \times 10^{13}$ s), making it possible to observe the transition into the sharper decay of the late-time regime at around $\tilde{t} = 100$ years. For the other cases, this transition occurs only at later times.

Interestingly, while all maneuvers exceed 20 nm at full aperture, when limiting the observation to a 90% aperture, the majority of cases remain below the 20-nm threshold. This occurs because the deformation originates at the telescope edges and propagates toward the center over time. The overall radial behavior of the deformation resembles an oscillating wave with diminishing amplitude toward the center. When observing with the full aperture, the maximal deformation decays monotonically, as it corresponds to the decay of the largest peak. However, the maximal deformation within the 90% aperture corresponds to the peak value included within that region at any given time. Since the wave propagates inward, we observe patterns of alternating peak decay with sudden increases corresponding to the arrival of new peaks.

We now turn to examine the effects of multiple sequential maneuvers on the deformation dynamics. For clarity and simplicity, hereafter we also fix the film's thickness to be $\tilde{h}_0 = 1$ mm and the angular velocity to be $\tilde{\omega}_0 = 50$ µrad/s (the conditions of configuration #2 in Fig. 5), and construct maneuver sequences from variations in the axis and magnitude of rotation. Within the timescales of interest, the deformation is limited to a narrow region close to the frame edges and cannot be discerned when plotting the deformation map of the entire telescope surface, as shown in Fig. 6(a). We thus adopt a transformed graphical representation of the surface that focuses on the outer 5% of the telescope's radius, as depicted in Fig. 6(b). The area contained within the inner 95% of the telescope's radius is purposely omitted and appears in white. In Fig. 6(c) we compare the dynamics of the maximal deformation for two maneuver sequences: The first (in orange) is a single slewing maneuver of 45° around the y axis. The second (in dashed black) is the same single slewing maneuver of 45° around the y axis, followed immediately by a 22.5° maneuver around the x axis and another −22.5° rotation back around the same axis—i.e., in both sequences the final position of the telescope is rotated by 45° around its original y axis. The actuation period is shown on a blue background, whereas the relaxation phase has a green background.

The first sequence behaves as one would expect from the results of Figs. 3 and 4—we see rapid buildup of the deformation to a level of 41 nm within approximately 4.5 h, followed by a slow decay wherein the deformation reduces to 14 nm within a week and to 5 nm within a year. However, as shown in Fig. 5 and depicted in the deformation map of Figs. 6(d) and 6(f), the deformation remains confined to the outer ring and does not yet penetrate the central aperture of the telescope.

The results of the second sequence, which consists of maneuvers around multiple axes, show that simple superposition cannot be applied in such cases. When the first maneuver, shared by the two sequences, is complete (the orange line begins to decay), the second maneuver (around the perpendicular axis) is initiated. Surprisingly, despite the active actuation, the deformation does not continue growing and instead exhibits a decay that follows closely that of the first sequence for approximately 2 hours. This is because the rotation around this perpendicular axis drives deformations in regions that were previously unperturbed. Two processes now occur simultaneously—the decay of the initial deformation and the buildup of the new (perpendicular) deformation. Initially, we see a decay of the maximal deformation since the new deformation has not yet increased sufficiently to change the global maxima on the surface. However, with time, the growing new deformation will surpass the decaying first deformation and will dictate the global maximum, again resulting in an increase of the maximal deformation. After one week of decay, the maximal deformation of the two cases is nearly identical, yet, as shown in Fig. 6(e), the surface of the second sequence is nearly axisymmetric, and this shape is maintained even at long times as shown in Fig. 6(g). From this

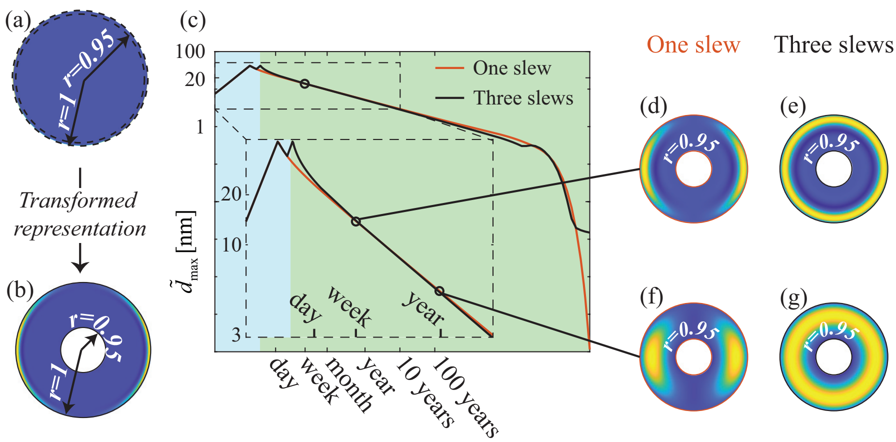

FIG. 6. Comparison of the liquid mirror deformation for two different sets of maneuvers of a 50-m diameter telescope with a 1 mm liquid layer. The first set involved a single 45° slewing maneuver around the y axis. The second set incorporates the same 45° maneuver around the y axis (as in the first set), followed by a subsequent 22.5° rotation around the x axis and a $-22.5°$ rotation back around the same axis. (a) The deformations of the liquid at a representative intermediate time, plotted over the full aperture. Since the deformation remains confined to a narrow region along the frame's edges it is not clearly visible in this representation. (b) Hereafter, we use a transformed graphical representation focusing only on the outer 5% of the telescope radius, with the inner 95% deliberately omitted. (c) The maximal deformation dynamics for the two cases, on a logarithmic timescale. The actuation period is represented with a blue background, and the relaxation phase with a green background. The inset focuses on the first few years to better illustrate the difference between the two sets of maneuvers investigated. Interestingly, since the additional maneuver occurs in a perpendicular direction, it does not increase the maximal deformation beyond its value in the first maneuver. [(d)–(g)] The surface deformation of the outer 5% of the telescope radius after one week [(d) and (e)] and one year [(f) and (g)]. While the maximal deformation in both is similar, the three-slews maneuver results in a more axisymmetric deformation.

point onward, the two cases continue decaying at approximately the same pace, with a very slight advantage to the second sequence that decays marginally faster. Hence, from an optical perspective, these results suggest that it may sometimes be more beneficial to add maneuvers in order to shape the surface into a geometry that is easier to correct optically.

The JWST performs approximately nine slewing maneuvers of several degrees each day [39]. Using this as reference, Fig. 7 shows the deformation of the liquid telescope within a 24-h period, as it undergoes a set of nine maneuvers, each of 5°, around a random rotation axis defined by the angle α in its x-y plane, as depicted in Fig. 7(a). Each maneuver lasts approximately 30 min and is then followed by approximately 2 h of observation time at which the telescope is at rest. Figure 7(c) presents the deformation during the first 24 h of actuation, showing the sequence of deformation buildup and relaxation between maneuvers. Depending on the direction of rotation, that is randomly assigned, we see that some actuations do not contribute significantly to the maximal deformation, as elucidated in Fig. 6. For comparison, we again present case #2 of Fig. 5—a single 45° maneuver over a 4.5-h period. Interestingly, the maximal deformation of the two cases after one day is comparable. Figure 7(d) presents the decay of the two cases over longer periods of time. After one day, the single maneuver case has already completed its rapid early decay phase and is entering the intermediate decay phase of $d_{\max} \sim t^{-1/4}$. The multiple maneuvers case, on the other hand, is just entering its early decay phase and thus decays more rapidly at that point. As a result, when both cases are well within their intermediate decay regime, the difference in maximal deformation between the two cases becomes more pronounced compared to the difference observed after one day.

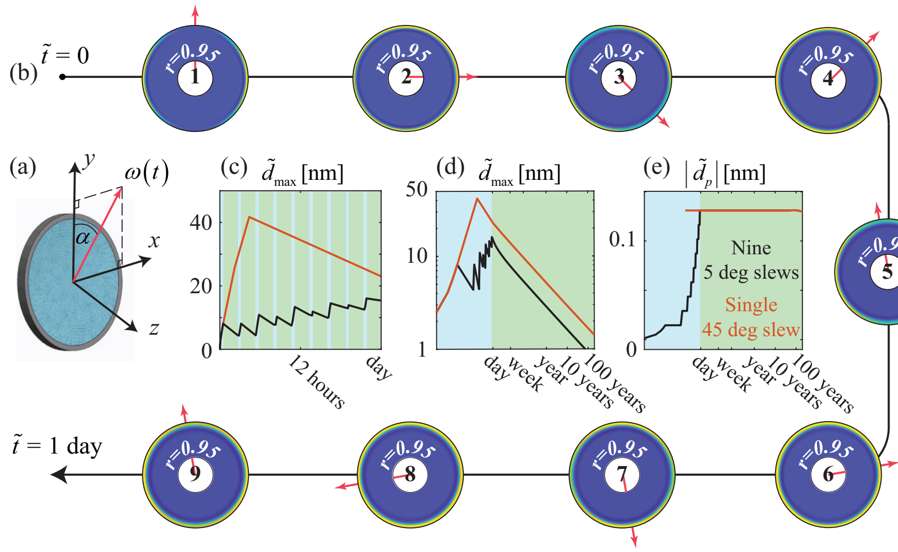

FIG. 7. Deformation dynamics of the 50-m diameter liquid mirror telescope over 24 h as a result of nine slewing maneuvers of 5° each around a randomly selected axis of rotation. (a) The axis of rotation (red arrow) is in the x-y plane and is defined by the angle relative to the y axis. (b) The deformation map after each of the nine slewing maneuvers, showing the deformation propagating toward the center. The axis of rotation of each maneuver is presented as a red arrow for each step. (c) The black curve corresponds to the deformation due to the nine maneuvers, showing the buildup and relaxation of deformation with each maneuver. As expected from Fig. 6, some rotations contribute minimally to the overall deformation. The orange curve presents, for comparison, the deformation due to a single 45° actuation and shows that multiple small maneuvers (in different directions) result in a smaller overall deformation. (d) The decay of the maximal deformation over longer time periods for the two cases. The decay rate is similar for both, with the initial difference in deformation persisting over time. (e) The piston deformation for both cases, noting that the incremental addition from each maneuver adds up to equal the total deformation seen in the single maneuver case.

Figure 7(e) presents piston deformations for the same cases and time periods. The piston deformation builds up with each maneuver and remains constant thereafter. The additional deformation in each maneuver is independent of the axis of rotation, and the total piston deformation can be simply summed up for the nine-maneuver case and is equal to that obtained from the single maneuver case. Figure 7(b) presents the deformation map of the mirror (within the 95% outer radius region), after each of the slewing maneuvers, and the axis of rotation for each step (red arrow). We see the deformation propagating toward the center, and, with time, becoming less sensitive to variations in the axis of rotation. Yet, since this is a small number of maneuvers which are not precisely in orthogonal directions, the surface deformations are never purely axisymmetric.

To gain a better understanding of mirror surface deformations during operation of a notional fluidic telescope, we studied a basic maneuver construct (Fig. 6) as well as a typical day's worth of maneuvers (Fig. 7). However, a realistic telescope would maneuver constantly throughout its lifetime—ideally tens of years. The results thus far clearly indicate that all maneuvers contribute to the deformation of the surface, and that relaxation driven by the surface tension force alone is too slow to recover the original spherical shape within a reasonable time. At the same time, we also see that the deformations propagate very slowly toward the center of the telescope. We next seek to examine the nature of deformations accumulated over a long period of continuous maneuvers and draw guidelines based on the understanding we gain from nondimensional analysis.

Figure 8 presents the deformation of a fluidic mirror over an actuation period of 10 years. While a realistic case consists of many small maneuvers each day, previous analysis (Fig. 7) shows that a

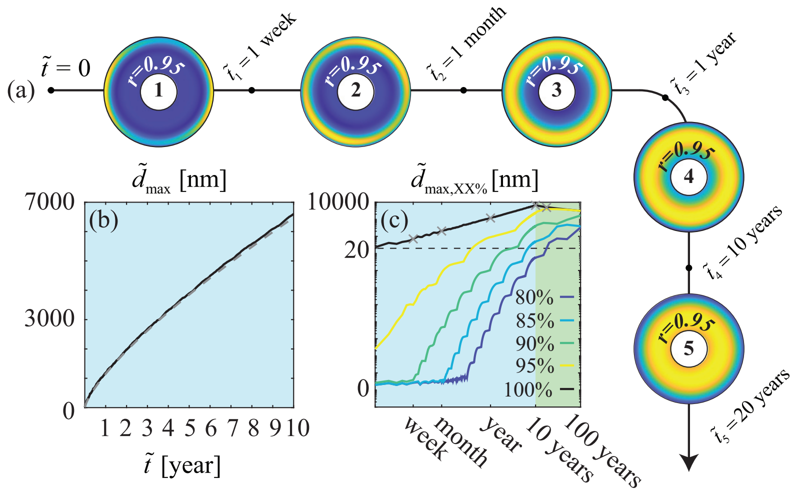

FIG. 8. Long-term deformation illustration of a fluidic mirror during a 10-year period, featuring a daily 45° slewing maneuver around a random in-plane rotation axis. (a) The mirror deformation at various times (A1, 1 week, A2, 1 month, A3, 1 year, A4, 10 years, A5, 20 years), showing the deformation becoming increasingly axisymmetric due to the variety of maneuver directions. (b) The maximum deformation across the telescope surface, accumulating to 6400 nm over 10 years (solid black line) and the analytical prediction Eq. (36) (gray dashed line). (c) The same deformation data on a logarithmic scale, together with the maximal deformations over smaller apertures, and during a hypothetical relaxation period. The deformation exceeds the selected critical threshold of 20 nm at the 95% radius (yellow line) after approximately six months, while for the 80% aperture (dark blue line), the maximal deformation remains below 20 nm for more than 20 years. The gray "x" marks correspond to the time points at which deformation maps are depicted.

simulation of a single large maneuver per day can serve as the worst-case scenario. Thus, to reduce the computational load, in our long-duration simulations we substitute a set of short maneuvers with a single large maneuver of 45° per day, around a different random in-plane rotation axis. Figure 8(a) presents the shape of the mirror surface as it evolves over time. Since the interface deformation is constructed of many rotations in different directions, in this case (consisting of 3650 maneuvers of 45° each) the deformation approaches an axisymmetric shape. Figure 8(b) shows the maximal deformation over the entire telescope surface, which builds up to 6400 nm during the 10-year operation period. Figure 8(c) presents the same data on a logarithmic scale and includes the maximal deformation for smaller apertures, as well as the behavior in a hypothetical relaxation period. Most importantly [as can also be observed in the colormaps of Fig. 8(a)], the deformation passes the threshold of 20 nm at the 95% and the 80% radius curves only after 6 months and 20 years, respectively—this deformation is the result of the earliest maneuvers that have just now reached this radius.

Interestingly, although the deformation pattern varies in both time and space, the maximal deformation follows the same trend discovered in the nondimensional analysis for a single maneuver $\tilde{d}_{max} = AC_{seq}t^{3/4}\tilde{h}_0$. While in this long-term operation the deformation does not grow monotonically, as predicted theoretically for a single maneuver, the theoretical trend still provides an excellent approximation, as seen in Figs. 8(b) and 8(c) (gray dashed line). To quantify this behavior, we introduce the constant C_{seq}, which represents a scaling factor linking the deformation from a single maneuver (obtained from the nondimensional analysis) to the cumulative deformation from many sequential maneuvers. This constant is defined by considering the fraction of time the telescope spends maneuvering, relative to the total period (actuation plus rest), and by averaging the effect of rotations around various axes.

For a large number of maneuvers, we assume that the resulting deformation is axisymmetric, similar to the outcome of rotating alternately about two perpendicular axes. Thus, for sequential operation, we propose the expression $C_{\text{seq}} = C_a\tilde{t}_a/2\tilde{t}_p$, where C_a is the constant found in the nondimensional analysis for a single actuation, $\tilde{t}_a$ is the actuation time, and $\tilde{t}_p$ is the full cycle period (actuation + rest). The factor of 2 accounts for the effective averaging over two perpendicular axes of rotation, assuming sufficient statistical coverage of orientation over time. Substituting into our model yields the theoretical prediction for the maximal deformation as a function of the fluidic mirror properties, as well as the slewing dynamics:

$$\tilde{d}_{\text{max,seq}} = C_a \frac{\tilde{t}_a}{2\tilde{t}_p} \frac{\tilde{\rho}\tilde{D}\tilde{\omega}^{5/4}\tilde{h}_0^{9/4}}{2\tilde{\sigma}^{1/4}} \left(\frac{\beta}{3\tilde{\mu}}\right)^{3/4}. \tag{36}$$

This expression captures the fact that deformation accumulates only during active slewing and benefits from the axisymmetric deformation profile resulting from randomly oriented maneuvers over a long period of time.

V. CONCLUDING REMARKS

In this paper we introduced a theoretical model and an analytical solution that describe liquid mirror dynamics for a fluidic space telescope under one of the most significant sources of perturbations—its slewing maneuvers required to change the observation point in space. Based on the model, we identified different regimes for both actuation and relaxation stages, providing valuable insights into the resulting deformation. For example, we observed that the maximal deformation at the actuation and relaxation stages scales as $t^{3/4}$ and $t^{-1/4}$, respectively. Furthermore, we derived simple expressions for the maximal deformation and piston deformation, highlighting their dependence on the liquid mirror properties and the maneuver characteristics. Equation (33) reveals that the maximal deformation of the film at actuation scales with the film thickness as $\tilde{h}_0^{9/4}$ and with the angular velocity as $\tilde{\omega}_0^{5/4}$. These results can serve as design guidelines for the telescope and its slewing plan.

Additionally, from an optical perspective, not only the maximal deformations matter, but also their spatial distribution. Our simulations predict that for a hypothetical telescope with a 50-m diameter, 1-mm-thick liquid mirror, the maximal deformation could reach several micrometers after 10 years of operation. However, within the inner 40 m (i.e., 80% of the aperture), the deformation remains under 20 nm even after 20 years. This difference highlights the importance of a dynamic model, as the viscoelastic timescales can be very long and may strongly affect the functionality of the overall system. These considerations may need to be incorporated in the design process of the telescope, where an obvious degree of freedom is to control the aperture used through an adjustable aperture stop (e.g., a mechanical iris), as is commonly done in many optical systems.

Another potential way of minimizing long-lasting mirror surface disturbances of a fluidic space telescope is through its concept of operations. In creating a sequence of astronomical observations, the expected surface deformation could be combined with other factors (e.g., timing, scientific value, and control effort required) in a multiobjective optimization in order to take maximum advantage of the remaining useful life of the telescope.

Ultimately, after sufficient use, the optical quality of the mirror surface will degrade. A "reset" procedure that restores the entire surface of a fluidic mirror to its original, precise geometry would be highly desirable. One possible option for such a procedure could be to combine linear acceleration and angular velocity around the z axis, as is done with ground-based liquid-mirror telescopes, shaping the liquid surface into a paraboloid. Other physical mechanisms include electromagnetic actuation similar to those employed in the Zenith program, or leveraging the thermocapillary effect to reshape the liquid and restore its optical properties [40].

The aforementioned actuation mechanisms can be incorporated into our finite-domain, thin-film model of fluidic mirrors as different source terms for Eq. (9). However, an additional step is needed when actuating via electromagnetic fields or temperature distributions across the mirror surface. In these cases the mirror surface evolution equation would need to be coupled with Maxwell's equations or an energy balance equation, respectively. In recent work [35], we used surface electrodes at the chamber bottom to apply DEP (electrical) interfacial forces to shape the liquid, while introducing the 1D non-self-adjoint thin-film model. We solved the electric field distribution numerically and, assuming small deformations, decoupled the two governing physical phenomena (electrostatics and fluid mechanics). We then used the numerical results as the source term for the thin-film equation. Importantly, we note that DEP stress and magnetic stress on a ferromagnetic fluid are very similar in nature. Both stresses originate from the differences in electric permittivity and magnetic susceptibility between the liquid and the air above it, respectively, and both apply force distributions at the interface in the normal direction. Thus, with the theoretical model suggested for magnetic stress at the interface [22], one should be able to readily incorporate this mechanism into our thin-film model.

ACKNOWLEDGMENTS

This project was funded by the European Union (ERC, Fluidic Shaping, 101044516). Views and opinions expressed are, however, those of the authors only and do not necessarily reflect those of the European Union or the European Research Council Executive Agency. Neither the European Union nor the granting authority can be held responsible for them. We also gratefully acknowledge funding from NASA Ames Center Innovation Fund (CIF), NASA Flight Opportunities program, NASA Innovative Advanced Concepts (NIAC) program, and the Israel Science Foundation Grant No. 2263/20. I.G. acknowledges the support of ISEF and the Azrieli Foundation.

DATA AVAILABILITY

The data that support the findings of this article are openly available [41].

APPENDIX A: PHYSICAL PARAMETERS OF THE FLUTE MISSION, NONDIMENSIONALIZATION, AND VALIDITY OF MODEL ASSUMPTIONS

This Appendix lists the baseline FLUTE parameters and nondimensionalizes the momentum equations in order to quantify the terms retained in the main text. The nondimensionalization identifies the Coriolis and Euler numbers and provides conditions under which they can be neglected.

1. FLUTE mission physical parameters

We here summarize the geometrical, material, and maneuver parameters used throughout the manuscript. The telescope frame has a diameter $\tilde{D} = 50$ m and radius of curvature $\tilde{R}_c = 300$ m. The thin liquid layer has nominal thickness $\tilde{h}_0$ in the range 10^{-3} to 10^{-2} m. We target an ionic liquid [14] with mass density $\tilde{\rho} \simeq 1.25 \times 10^3$ kg m^{-3}, kinematic viscosity $\tilde{\nu} \simeq 10^{-4}$ m^2 s^{-1}, and surface tension $\tilde{\sigma} \simeq 70$ mN m^{-1}. The characteristic slewing angular velocity is taken in the range $\tilde{\omega}_0 = 10$ to 100 µrad s^{-1}.

2. Nondimensionalization of the momentum equations

We repeat here the lubrication form of the momentum equations [Eqs. (5a) and (5b)] obtained in the main text

$$\tilde{\nabla}_s \tilde{p} = \tilde{\mu} \frac{\partial^2 \tilde{\mathbf{u}}_s}{\partial \tilde{z}^2} + \tilde{\rho}(-2\tilde{\omega}\tilde{w} - \dot{\tilde{\omega}}\tilde{z} + \tilde{\omega}^2 \tilde{x})\hat{\mathbf{x}}, \tag{A1}$$

$$\frac{\partial \tilde{p}}{\partial \tilde{z}} = \tilde{\rho}(\tilde{\omega}^2 \tilde{z} + 2\tilde{\omega}\tilde{u} + \dot{\tilde{\omega}}\tilde{x} - \tilde{g}). \tag{A2}$$

TABLE I. Summary of key nondimensional parameters of the FLUTE baseline design.

Quantity	Definition	FLUTE value or range
Small slope	$\epsilon = \tilde{D}/(2\tilde{R}_c)$	8.3×10^{-2}
Aspect ratio	$\varepsilon = 2\tilde{h}_0/\tilde{D}$	4×10^{-5} to 4×10^{-4}
Reduced Reynolds	$\mathrm{Re}_r = (\frac{\tilde{\omega}_0 \tilde{h}_0^2}{\tilde{\nu}})^2$	10^{-14} to 10^{-8}
Coriolis number	$\Pi_{\mathrm{Co}} = \varepsilon\tilde{\omega}_0\tilde{h}_0^2/\tilde{\nu} = \varepsilon\sqrt{\mathrm{Re}_r}$	10^{-12} to 10^{-8}
Euler number	$\Pi_{\mathrm{Eu}} = \tilde{\alpha}_c\varepsilon/\tilde{\omega}_0^2$	$\ll$1 by design

We introduce the following scales and nondimensional variables:

$$\tilde{x} = (\tilde{D}/2)x, \quad \tilde{z} = \tilde{h}_0 z, \quad \varepsilon = 2\tilde{h}_0/\tilde{D}, \quad \tilde{u} = \tilde{U}_s u, \quad \tilde{v} = \tilde{U}_s v,$$
$$\tilde{w} = \varepsilon\tilde{U}_s w, \quad \tilde{\omega} = \tilde{\omega}_0\omega, \quad \dot{\tilde{\omega}} = \tilde{\alpha}_c\dot{\omega}, \quad \tilde{p} = \tilde{P}_c p.$$

Substituting these parameters into Eq. (A1) and dividing by the prefactor multiplying the viscous terms, $\tilde{\mu}\tilde{U}_s/\tilde{h}_0^2$, yields

$$\frac{\tilde{P}_c\tilde{h}_0^2}{\tilde{\mu}\tilde{U}_s(\tilde{D}/2)}\nabla_s p = \frac{\partial^2 u_s}{\partial z^2} - \left(2\,\varepsilon\frac{\tilde{\omega}_0\tilde{h}_0^2}{\tilde{\nu}}\,\omega w - \frac{\tilde{\alpha}_c\tilde{h}_0^3}{\tilde{\nu}\tilde{U}_s}\,\dot{\omega}z + \frac{\tilde{\omega}_0^2(\tilde{D}/2)\tilde{h}_0^2}{\tilde{\nu}\tilde{U}_s}\,\omega^2 x\right)\hat{\mathbf{x}}. \tag{A3}$$

We choose the velocity and pressure scales as $\tilde{U}_s = \frac{\tilde{\omega}_0^2(\tilde{D}/2)\tilde{h}_0^2}{\tilde{\nu}}$ and $\tilde{P}_c = \tilde{\rho}\tilde{\omega}_0^2(\tilde{D}/2)^2$, such that the centrifugal and pressure gradient terms are of order one. The nondimensional in plane momentum equation thus simplified to

$$\nabla_s p = \frac{\partial^2 u_s}{\partial z^2} - (2\,\Pi_{\mathrm{Co}}\,\omega w - \Pi_{\mathrm{Eu}}\,\dot{\omega}z + \omega^2 x)\hat{\mathbf{x}}, \tag{A4}$$

where we define the Coriolis and Euler nondimensional numbers as

$$\Pi_{\mathrm{Co}} = \varepsilon\frac{\tilde{\omega}_0\tilde{h}_0^2}{\tilde{\nu}}, \quad \Pi_{\mathrm{Eu}} = \frac{\tilde{\alpha}_c\,\varepsilon}{\tilde{\omega}_0^2}. \tag{A5}$$

Substituting the same scales into Eq. (A2) yields

$$\frac{\partial p}{\partial z} = \varepsilon^2\omega^2 z + 2\Pi_{\mathrm{Co}}\,\omega u + \varepsilon\Pi_{\mathrm{Eu}}\,\dot{\omega}x - \frac{\tilde{g}\,\tilde{h}_0}{\tilde{\omega}_0^2\,(\tilde{D}/2)^2}. \tag{A6}$$

As mentioned in the main text, we keep gravity in the model derivation for two main reasons: first, for validation of the film dynamics predicted by the theoretical model with experiments that we perform on Earth and, second, because this theoretical framework applies to any pinned thin film in a circular-chamber configuration.

Table I lists the nondimensional numbers and their values for the FLUTE baseline design. We evaluate the assumptions using the upper bounds in Table I. The lubrication approximation requires $\varepsilon \ll 1$ and $\mathrm{Re}_r \ll 1$. The Coriolis number can be expressed as $\Pi_{\mathrm{Co}} = \varepsilon\sqrt{\mathrm{Re}_r}$ and is therefore also small. Last, neglecting the Euler terms requires $\Pi_{\mathrm{Eu}} \ll 1$, which provides the requirement on the angular acceleration of the telescope $\tilde{\alpha}_c \ll \tilde{\omega}_0^2/\varepsilon$.

APPENDIX B: AUXILIARY FUNCTION DERIVATION

This Appendix details the steps needed to derive the auxiliary function $f(r,\theta)$ used in Eq. (14) and the polynomial coefficients C_n in Eq. (15). The goal is to eliminate the azimuthally dependent boundary forcing. We introduce the transformed deformation variable $\delta = d - f(r,\theta)\,g(t)$ and then choose f and g so that δ satisfies homogeneous boundary conditions. For simplicity of the resulting algebraic expressions, we present here the case of $\mathrm{Bo} = 0$, but the same procedure can be applied to obtain f and g for nonzero values of Bo. We start with the governing equation [Eq. (9)] for the case of $\mathrm{Bo} = 0$,

$$d_t + \nabla_s^4 d = -A\,\omega^2(t), \tag{B1}$$

and the boundary conditions at $r = 1$, for all θ and $t \geqslant 0$, are

$$\begin{aligned} &d = 0, \\ &d_{rrr} - d_r + d_{rr} - 2d_{\theta\theta} + d_{r\theta\theta} = -A\,\omega^2(t)\cos^2\theta. \end{aligned} \tag{B2}$$

To homogenize the no-penetration boundary condition in Eq. (B2) we define the transformed deformation variable,

$$\delta(r,\theta,t) = d(r,\theta,t) - f(r,\theta)\,g(t), \tag{B3}$$

where $f(r,\theta)$ is a prescribed spatial auxiliary function and $g(t)$ is a prescribed auxiliary temporal function. Substituting Eq. (B3) into Eq. (B1) gives the evolution equation for δ,

$$\delta_t + \nabla_s^4\delta = -g_t\,f(r,\theta) - g(t)\big(A + \nabla_s^4 f\big), \tag{B4}$$

and substituting Eq. (B3) into the boundary conditions in Eq. (B2) gives the boundary conditions for δ at $r = 1$, for all θ and $t \geqslant 0$,

$$\begin{aligned} &\delta(1,\theta,t) = -f(1,\theta)\,g(t), \\ &\delta_{rrr} - \delta_r + \delta_{rr} - 2\delta_{\theta\theta} + \delta_{r\theta\theta} = -\omega^2(t)A\cos^2\theta - g(t)(f_{rrr} - f_r + f_{rr} - 2f_{\theta\theta} + f_{r\theta\theta}). \end{aligned} \tag{B5}$$

We set $g(t) = \omega^2(t)$ and find $f(r,\theta)$ such that the boundary conditions in Eq. (B5) are homogeneous. This requires

$$f(1,\theta) = 0, \quad f_{rrr} - f_r + f_{rr} - 2f_{\theta\theta} + f_{r\theta\theta} = -A\cos^2\theta \quad \text{at } r = 1, \tag{B6}$$

which reduces Eq. (B5) to

$$\delta(1,\theta,t) = 0, \quad \delta_{rrr} - \delta_r + \delta_{rr} - 2\delta_{\theta\theta} + \delta_{r\theta\theta} = 0. \tag{B7}$$

We assume a separable form for f,

$$f(r,\theta) = \mathcal{F}(\theta)\,\mathcal{G}(r), \quad \mathcal{G}(r) = \sum_{n=0}^{N} C_n r^n. \tag{B8}$$

Substituting Eq. (B8) into the second condition in Eq. (B6) yields an ordinary differential equation for $\mathcal{F}$,

$$B_1\mathcal{F} + B_2\mathcal{F}_{\theta\theta} = -\frac{A}{2}(1 + \cos 2\theta), \tag{B9}$$

where $B_1 = \mathcal{G}'''(1) + \mathcal{G}''(1) - \mathcal{G}'(1)$ and $B_2 = \mathcal{G}'(1) - 2\mathcal{G}(1)$ depend only on $\mathcal{G}$ and its derivatives at $r = 1$. Imposing 2π-periodicity of $\mathcal{F}$ and $\mathcal{F}_\theta$ gives

$$\mathcal{F}(\theta) = -\frac{A}{2}\left(\frac{1}{B_1} + \frac{\cos(2\theta)}{B_1 - 4B_2}\right). \tag{B10}$$

We determine the polynomial order N and the coefficients C_n by satisfying the boundary conditions, enforcing regularity at $r = 0$, and enforcing mass conservation. For $\mathrm{Bo} = 0$, the lowest order satisfying these requirements is $N = 4$.

The right-hand side of Eq. (B4) contains $f(r,\theta)$ and $A + \nabla_s^4 f$. We require that both be regular at $r = 0$, that is, contain no negative powers of r.

For Bo $= 0$, substituting Eq. (B8) into $A + \nabla_s^4 f$ yields

$$\frac{A(C_1 - 9C_3)}{C_1 - 9C_3 - 32C_4} + \frac{A\left(\frac{C_1}{C_1-9C_3-32C_4} - \frac{9C_1\cos(2\theta)}{8C_0+3C_1+5C_3+24C_4}\right)}{2r^3} + \frac{A\left(\frac{9C_3}{C_1-9C_3-32C_4} + \frac{15C_3\cos(2\theta)}{8C_0+3C_1+5C_3+24C_4}\right)}{2r}. \tag{B11}$$

Eliminating the negative powers of r in Eq. (B11) requires $C_1 = C_3 = 0$, which in this case leads to $A + \nabla_s^4 f \equiv 0$.

The first condition in Eq. (B6) gives

$$C_0 + C_1 + C_2 + C_3 + C_4 = 0. \tag{B12}$$

We also impose the mass conservation constraint on f, ensuring that the forcing terms satisfy the zero integral constraint required by the eigenfunction basis,

$$\int_0^{2\pi}\int_0^1 f(r,\theta)\, r\, dr\, d\theta = 0, \qquad \Longrightarrow \qquad 30C_0 + 20C_1 + 15C_2 + 12C_3 + 10C_4 = 0. \tag{B13}$$

Solving for C_n yields

$$C_0 = \tfrac{1}{3}, \quad C_1 = 0, \quad C_2 = -\tfrac{4}{3}, \quad C_3 = 0, \quad C_4 = 1. \tag{B14}$$

With $\mathcal{G}(r)$ fixed, we evaluate B_1 and B_2 and obtain $f(r,\theta)$.

$$f(r,\theta) = -\frac{A}{960}\,(1 - 4r^2 + 3r^4)\,(5 + 6\cos(2\theta)). \tag{B15}$$

Summary and general recipe for nonzero Bond numbers

The auxiliary function is introduced to remove the azimuthally dependent forcing from the boundary conditions by transforming the deformation as $\delta = d - f(r,\theta)\,g(t)$, with $g(t) = \omega^2(t)$. The function $f(r,\theta)$ is then chosen so that δ satisfies homogeneous boundary conditions, while the forcing terms generated in the evolution equation for δ, Eq. (B4), satisfy the same constraints required by the eigenfunction expansion.

In practice, f is constructed by enforcing the following conditions:

(1) *Homogeneous boundary conditions for δ:* Choose f such that Eq. (B6) holds. Together with $g(t) = \omega^2(t)$, this reduces the boundary conditions in Eq. (B5) to the homogeneous form in Eq. (B7).

(2) *Regularity at the origin:* Require that f and $A + \nabla_s^4 f - \mathrm{Bo}\nabla_s^2 f$ contain no negative powers of r.

(3) *Zero integral constraint:* We impose the mass conservation constraint on both f and the expression $A + \nabla_s^4 f - \mathrm{Bo}\nabla_s^2 f$. In the special case where Bo $= 0$, the constraint is required only for f, as $A + \nabla_s^4 f$ vanishes completely once the regularity condition is applied.

To construct $f(r,\theta)$, we take the separable form $f(r,\theta) = \mathcal{F}(\theta)\mathcal{G}(r)$ with $\mathcal{G}$ being a polynomial as in Eq. (B8). The coefficients C_n are then determined from the boundary conditions in Eq. (B6), the regularity requirement at $r = 0$, and the zero integral constraint. The resulting coefficients for the general case are reported in Eq. (15).

[1] J. C. Tarter, The search for extraterrestrial intelligence (SETI), Annu. Rev. Astron. Astrophys. **39**, 511 (2001).

[2] D. A. Vakoch and M. F. Dowd, eds., *The Drake Equation: Estimating the Prevalence of Extraterrestrial Life through the Ages*, Cambridge Astrobiology Vol. 8 (Cambridge University Press, Cambridge, UK, 2015).

[3] D. J. D. Marais *et al.*, Remote sensing of planetary properties and biosignatures on extrasolar terrestrial planets, Astrobiology **2**, 153 (2002).

[4] S. Seager, The future of spectroscopic life detection on exoplanets, Proc. Natl. Acad. Sci. USA **111**, 12634 (2014).

[5] O. Ganel, R. Rivera, J. Falker, N. Siegler, B. Crill, and M. R. Perez, NASA strategic astrophysics technology investments: A decade of benefits, outlook informed by the 2020 decadal survey, in *Advances in Optical and Mechanical Technologies for Telescopes and Instrumentation V*, Proceedings of SPIE Vol. 12188 (SPIE, Bellingham, WA, 2022), pp. 57.

[6] Q. Gong *et al.*, Optical design of the Extreme Coronagraph for Living Planetary Systems instrument for the LUVOIR mission study, J. Astron. Telesc. Instrum. Syst. **5**, 025002 (2019).

[7] Committee for a Decadal Survey on Astronomy and Astrophysics 2020 (Astro2020), Space Studies Board, Board on Physics and Astronomy, Division on Engineering and Physical Sciences, National Academies of Sciences, Engineering, and Medicine, *Pathways to Discovery in Astronomy and Astrophysics for the 2020s* (National Academies Press, Washington, DC, 2023).

[8] J. P. Gardner *et al.*, The James Webb Space Telescope, Space Sci. Rev. **123**, 485 (2006).

[9] C. J. Burrows, J. A. Holtzman, S. M. Faber, P. Y. Bely, H. Hasan, C. R. Lynds, and D. Schroeder, The imaging performance of the Hubble Space Telescope, Astrophys. J. **369**, L21 (1991).

[10] L. Team, The LUVOIR mission concept study final report, Technical Report (NASA Goddard Space Flight Center, 2019) nASA/GSFC.

[11] K. Colon, R. Massey, and E. Newton, Ariane 5 fairing preparations for James Webb Space Telescope, Technical Report NASA TRS 20230002781 (NASA Technical Reports Server, Washington, DC, 2023).

[12] M. R. Bolcar *et al.*, The Large UV/Optical/Infrared Surveyor (LUVOIR): Decadal mission concept design update, in *UV/Optical/IR Space Telescopes and Instruments: Innovative Technologies and Concepts VIII*, Proc. SPIE Vol. 10398 (SPIE, Bellingham, WA, 2017), p. 1039809.

[13] M. Nayak, D. Brousseau, A. Childers, and K. Iyer, Zenith: Darpa's liquid mirror telescope program, in *Advances in Optical and Mechanical Technologies for Telescopes and Instrumentation VI*, Proc. SPIE Vol. 13100 (SPIE, Bellingham, WA, 2024), pp. 994.

[14] O. Luria *et al.*, Shaping a gallium alloy and an ionic liquid into spherical mirrors for future liquid-based telescopes—experimental setup and demonstration in parabolic flights, J. Astron. Telesc. Instrum. Syst. **10**, 044010 (2024).

[15] N. C. Lima, K. Mishra, and F. Mugele, Aberration control in adaptive optics: A numerical study of arbitrarily deformable liquid lenses, Opt. Express **25**, 6700 (2017).

[16] H. C. King, *The History of the Telescope* (Courier Corporation, Glouster, MA, 2003).

[17] D. Olsson-Steel, A note on the history of the liquid mirror telescope, J. R. Astron. Soc. Can. **80**, 128 (1986).

[18] E. F. Borra, Liquid mirror telescopes—Present and future, Publ. Astron. Soc. Pac. **99**, 1229 (1987).

[19] E. F. Borra, Liquid mirrors, Sci. Am. **270**, 76 (1994).

[20] M. Hayez, *Bulletins de l'Académie Royale des Sciences, des Lettres et des Beaux-Arts de Belgique* (Imprimeur de l'Académie Royale de Belgique, Brussels, 1898).

[21] M. Nayak, S. Basu, and K. Iyer, Zenith: A DARPA liquid mirror technology development program, in *Photonic Instrumentation Engineering XI*, Proc. SPIE Vol. 12893 (SPIE, Bellingham, WA, 2024), pp. 23–29.

[22] N. Rowlands *et al.*, Development of a self-assembling ferrofluidic ionic liquid mirror, in *Advances in Optical and Mechanical Technologies for Telescopes and Instrumentation VI*, Proc. SPIE Vol. 13100 (SPIE, Bellingham, 2024), p. 131007H.

[23] NASA, What is the fluidic telescope? (2023), available at https://www.nasa.gov/science-research/astrophysics/what-is-the-fluidic-telescope/.

[24] L. Hall, Fluidic telescope (FLUTE): Enabling the next generation of large space observatories (2023), available at https://www.nasa.gov/general/fluidic-telescope-flute-enabling-the-next-generation-of-large-space-observatories/.

[25] NASA, NIAC 2023 phase I and phase II selections (2023), available at https://www.nasa.gov/general/niac-2023-phase-i-and-phase-ii-selections/.

[26] V. Frumkin and M. Bercovici, Fluidic shaping of optical components, Flow **1**, E2 (2021).

[27] M. Elgarisi, V. Frumkin, O. Luria, and M. Bercovici, Fabrication of freeform optical components by fluidic shaping, Optica **8**, 1501 (2021).

[28] K. Banerjee, P. Rajaeipour, Ç. Ataman, and H. Zappe, Optofluidic adaptive optics, Appl. Opt. **57**, 6338 (2018).

[29] M. Sohmen, J. D. Muñoz Bolaños, P. Rajaeipour, M. Ritsch-Marte, Ç. Ataman, and A. Jesacher, Optofluidic adaptive optics in multi photon microscopy, Biomed. Opt. Express **14**, 1562 (2023).

[30] A. Dorn, H. Zappe, and Ç. Ataman, Conjugate adaptive optics extension for commercial microscopes, Adv. Photon. Nexus **3**, 056018 (2024).

[31] P. D. Howell, Surface-tension-driven flow on a moving curved surface, J. Eng. Math. **45**, 283 (2003).

[32] L. G. Leal, *Advanced Transport Phenomena: Fluid Mechanics and Convective Transport Processes* (Cambridge University Press, Cambridge, UK, 2007).

[33] A. Oron, S. H. Davis, and S. G. Bankoff, Long-scale evolution of thin liquid films, Rev. Mod. Phys. **69**, 931 (1997).

[34] R. V. Craster and O. K. Matar, Dynamics and stability of thin liquid films, Rev. Mod. Phys. **81**, 1131 (2009).

[35] I. Gabay, V. Bacheva, D. Ilssar, M. Bercovici, A. Ramos, and A. Gat, Dynamics of fixed-volume pinned films—dealing with a non-self-adjoint thin-film problem, J. Fluid Mech. **969**, A17 (2023).

[36] E. A. Coddington and N. Levinson, *Theory of Ordinary Differential Equations* (Tata McGraw-Hill Education, New York, 1955).

[37] I. Gabay, F. Paratore, E. Boyko, A. Ramos, A. Gat, and M. Bercovici, Shaping liquid films by dielectrophoresis, Flow **1**, E13 (2021).

[38] Z. Zheng, M. A. Fontelos, S. Shin, M. C. Dallaston, D. Tseluiko, S. Kalliadasis, and H. A. Stone, Healing capillary films, J. Fluid Mech. **838**, 404 (2018).

[39] Space Telescope Science Institute, Observing schedules (2023), available at https://www.stsci.edu/home/jwst/science-execution/observing-schedules.

[40] R. Eshel, V. Frumkin, M. Nice, O. Luria, B. Ferdman, N. Opatovski, K. Gommed, M. Shusteff, Y. Shechtman, and M. Bercovici, Programmable thermocapillary shaping of thin liquid films, Flow **2**, E27 (2022).

[41] I. Gabay, O. Luria, E. Balaban, A. D. Gat, and M. Bercovici, MATLAB code for “Fluid dynamics of a liquid mirror space telescope” (2026), available at https://github.com/IsraelGabay1/FLUTE-liquid-mirror-dynamics.